Research on Engineering Structures & Materials
www.jresm.org
MIM Research Group

Research Article

Gait phase manifold modulation mechanism of quadruped robot based on nonlinear differential geometry and Hopf bifurcation analysis

Mengqian Jiao [*,a]

College of General Education, Guilin Institute of Information Technology, Guilin, China

Article Info

Article History:

Received 23 July 2026

Accepted 09 Oct 2026

Keywords:

Quadruped robot;
Gait phase manifold modulation;
Nonlinear differential geometry analysis;
Hopf bifurcation analysis;
Central pattern generator

Abstract

To address the difficulty of balancing diversity and smoothness in gait phase manifold modulation for quadruped robots, this study proposes a modulation mechanism based on nonlinear differential geometry and Hopf bifurcation analysis. A central pattern generator (CPG)-Hopf oscillator network with environmental force feedback is established, and a phase perturbation dynamics model is constructed using polar coordinate transformation and contact force feedback. Nonlinear differential geometry defines the limiting circulation shape, while geodesic distance and Floquet theory analyze gait stability and switching paths. The manifold topological transition is driven by Hopf bifurcation conditions, with parameter optimization and Lyapunov functions enabling smooth gait modulation. This method assumes rigid grounding and ideal phase tracking. The differential geometry framework is applicable to low dimensional limit cycle manifolds and locally smooth gait transitions. Experimental results show that the frequency error is concentrated in the 0.4 Hz-1.1 Hz range, with a peak density of 0.8 Hz. The overall gait switching success rate across different terrain categories exceeds 96.0%, and the stability margin during the gait cycle exceeds 7.9 cm. When the time increases from 1.0 s to 5.0 s, the forward speed rises from 0.60 m/s to 1.20 m/s, an increase of 0.60 m/s. The proposed method improves gait adaptability and motion stability of quadruped robots in unstructured environments.

© 2026 MIM Research Group. All rights reserved.

1. Introduction

Quadruped robots have excellent terrain adaptability and movement flexibility and have great application potential in areas such as disaster relief, planetary exploration, material transportation, and special services. Gait generation and control are at the core of the motion capabilities of quadruped robots, directly determining their mobility efficiency, stability and energy consumption levels in complex unstructured environments [1]. However, most of the existing research on gait control has focused mainly on gait sequence planning, foot-end trajectory generation and feedback-based stability control, lacking exploration of the inherent phase dynamics characteristics of gait and its systematic modulation mechanism [2]. Traditional methods often rely on linearized approximations or simplified dynamic models, making it difficult to fully describe the high-dimensional nonlinear characteristics of gait patterns in complex terrains [3]. Nonlinear differential geometry analysis can study the phase dynamics equations on manifolds, thereby more essentially describing the constraints and coordination between phase variables and transforming the gait transition problem into a trajectory planning and tracking problem on manifolds [4]. Hopf bifurcation analysis can achieve natural and dynamic transitions between gaits by adjusting

*Corresponding author: jiao_mengqian@outlook.com
[a]orcid.org/0009-0003-8746-8844
DOI: http://dx.doi.org/10.17515/resm2026-2027vk0723rs

parameters to enable the system to transition from one limit loop attractor to another through bifurcation [5].

Therefore, to enhance the autonomous adaptability and robustness of quadruped robot gaits in response to sudden disturbances and complex terrains, a gait phase manifold modulation mechanism for quadruped robots based on nonlinear differential geometry and Hopf bifurcation analysis is proposed in this study. A Central Pattern Generator (CPG) - Hopf oscillator network model integrating environmental force feedback is first established. Next, using nonlinear differential geometry tools, the gait pattern is abstracted as a limiting circulation shape, and its geometric properties and stability are analyzed. When environmental changes trigger parameter perturbations and satisfy Hopf bifurcation conditions, manifold topological transitions occur in the system to achieve gait mode transitions. Furthermore, the precise regulation of the target gait is completed by combining phase response mapping and parameter optimization. After the global stability verification with the Lyapunov function, a robust gait adapted to the new environment is finally generated.

The theoretical contributions are threefold. First, central manifold reduction reduces the eight-dimensional CPG-Hopf state space to a low-dimensional limit-cycle manifold while retaining the two-dimensional amplitude-phase dynamics near the Hopf bifurcation. Second, a differential mapping is defined from the eight-dimensional CPG manifold to the robot joint space as $\Phi_{\mathrm{CPG}\to q}$: $\mathcal{M}_{\mathrm{CPG}} \subset \mathbb{R}^8 \to Q \subset \mathbb{R}^{n_q}$. Its limit-cycle submanifold is $\mathcal{M}_{LC} = \{X \in \mathbb{R}^8 \mid X = \gamma(\phi; p),\ \phi \in S^1\}$. In local phase-amplitude coordinates ϕ_i and r_i, the tangent map is $D\Phi_{\mathrm{CPG}\to q} = [J_i(\phi_i)\ \partial q_i/\partial r_i]$, and the joint trajectory follows $q_i(t) = q_{i,0} + J_i(\phi_i) r_i(t) + g_i(r, \dot{r})$. This mapping links oscillator phase and amplitude to joint motion and preserves manifold geometry. Third, geodesic distance on the reduced manifold and Floquet exponents provide a quantitative criterion for gait stability and switching path selection, which avoids the slow coupling evolution of conventional CPG models and supports rapid smooth gait modulation.

2. Related Work

The coordination of the gait phase relationship of quadruped robots directly determines their propulsion efficiency and dynamic balance ability. Therefore, the study of the gait phase manifold modulation mechanism of quadruped robots is of great significance. Prasad H K H et al. proposed a geometric mechanics-based adjustable bigait design framework in response to the limited on-board computing power of micro-legged robots. The results showed that the method could precisely control speed and steering [6]. Song Z et al. proposed a central pattern generation controller based on time-delay coupled van der Boer oscillators for the problem of gait generation and control in quadruped robots, which effectively generated diverse rhythm signals [7]. Liu X et al. proposed an end-to-end reinforcement learning framework based on gait encoders and generators to address the difficulty of multi-gait switching and terrain adaptation in blind quadruped robots. The method could achieve smooth gait switching based solely on proprioception [8]. Chen C et al. proposed a two-layer optimization method that co-optimizes morphological parameters and control strategies to address the issue of small legged robots sacrificing workspace due to limited actuator degrees of freedom. The method could efficiently discover the optimal form and gait [9]. Huang Y et al. proposed a control scheme that integrates Kalman filtering terrain perception and impedance stiffness adaptation to address the problem that quadruped robots are vulnerable to high-frequency jitter and torque deviation in unstructured terrain. The results showed that the method could effectively reduce transient oscillations [10].

Modern quadrupedal robotics has adopted model predictive control, whole-body control and deep reinforcement learning as academic and industrial benchmarks. Model Predictive Control (MPC) and Whole-Body Control (WBC) stacks on MIT Cheetah, ANYmal and Unitree platforms solve contact-consistent whole-body dynamics over a receding horizon and enforce friction cone, torque and kinematic constraints. They achieve high bandwidth and strong disturbance rejection but require accurate models, high-rate quadratic programming and substantial onboard computation [11]. Deep Reinforcement Learning (RL) locomotion policies learn terrain-aware gaits from proprioception and exteroception and demonstrate robust sim-to-real transfer. Their limitations

include sample complexity, policy inference latency and limited interpretability of phase coordination [12]. Central Pattern Generator (CPG)-based manifold modulation has lower computational load, explicit limit-cycle phase structure and fast bifurcation-driven switching. Its trade-off is weaker global optimality and reduced adaptation to unmodeled terrain. The proposed method therefore complements MPC, WBC and RL by providing a low-dimensional phase manifold that can serve as a smooth reference generator or safety layer.

Many scholars at home and abroad have conducted in-depth research and application of nonlinear differential geometry and Hopf bifurcation analysis. Eclerova V et al. proposed a method of replacing harmonic terms with supercritical Hopf bifurcation specifications to address the difficulty of bifurcation extension in nonlinear systems caused by phase unbounded properties. The results showed that the method could effectively overcome the computational barrier of phase unboundedness [13]. Liu D et al. proposed an analysis method combining the implicit function theorem with Hopf bifurcation for the problem of non-uniform steady-state solutions and periodic solutions of spatial heterogeneous time-delay reactivity - diffusion - convection systems. The method precisely characterized the bifurcation direction and stability of the solution [14]. Mustafa S A et al. proposed an analytical method based on averaging and polynomial system equilibrium point analysis for the existence of periodic solutions for Hopf and zero-Hopf bifurcations in the four-dimensional Lotka-Volterra model. This method could effectively construct the existence conditions of periodic solutions [15]. Shaik J et al. proposed a method combining double Hopf bifurcation analysis and multi-scale perturbation for time-delay nonlinear dynamics problems in roll motion control of low freeboard ship models. The method could accurately reveal the stable equilibrium, the small amplitude limit loop and the instability region [16]. Achouri H et al. proposed an explicit formula based on central manifold reduction and normal form method for the complex problem of zero-Hopf bifurcation gauge form calculation caused by multiple delays in neutral functional differential equations. This method could effectively simplify higher-order calculations [17].

To integrate phase response curve and center manifold theory into the related work, this study adds a methodological comparison of CPG phase-space topology and manifold control. Existing methods are grouped into four families, namely PRC phase resetting, center manifold reduction, Hopf bifurcation modulation and coupled CPG synchronization. Their convergence behavior during phase modulation is compared mathematically. PRC phase resetting treats the limit cycle as a phase oscillator with isochrons and uses the phase sensitivity function $Z(\varphi)$. Its first-order phase shift is $\Delta\varphi = \int Z(\varphi)p(\varphi)dt + O(\varepsilon^2)$, and the residual error decays with the Floquet multiplier $|p|^n$. Center manifold reduction projects the high-dimensional CPG dynamics onto a low-dimensional invariant manifold. Near a Hopf point the amplitude follows $A\sim\mathrm{sqrt}\left((\mu-\mu_c)/l_1\right)$, and the convergence time scales as $\tau\sim 1/\,Re\,\lambda\,(\mu)$. Hopf bifurcation modulation changes the phase-space topology when $Re\,\lambda\,(\mu)$ crosses zero. The switching path converges at $O(|\mu-\mu_c|^{1/2})$ near criticality. Coupled CPG synchronization forms a phase-locking manifold and converges exponentially as $exp\left(-\lambda_{\mathrm{gap}}t\right)$, where λ_{gap} is the spectral gap of the coupling matrix. These results show that PRC theory quantifies instantaneous phase sensitivity, center manifold theory gives reduced-order convergence near bifurcation, Hopf bifurcation supplies the topological switching condition, and coupled CPG synchronization ensures multi-limb coordination. Their combination supports fast and smooth gait phase manifold modulation in quadruped robots. Compared with PRC phase resetting, center manifold reduction gives a lower-dimensional and more interpretable convergence estimate near the critical point. Compared with Hopf bifurcation modulation alone, the combined framework adds a quantitative phase sensitivity measure and a reduced-order stability condition. Compared with coupled CPG synchronization, it provides an explicit topological transition criterion rather than only phase-locking. This comparison provides a methodological benchmark for the proposed mechanism and avoids a purely chronological literature list.

In summary, the existing research has a good effect on motion control for quadruped robots, but its phase adjustment relies on the slow evolution of coupling terms, making it difficult to achieve fast and smooth straddle-gait modulation. Nonlinear differential geometry analysis abstracts the state space of the gait phase system of the quadruped robot as a smooth manifold; Hopf bifurcation

analysis models the rhythmic motion of each leg of the robot as a network of nonlinear oscillators. Therefore, a quadruped robot gait phase manifold modulation mechanism based on nonlinear differential geometry and Hopf bifurcation analysis is proposed in the study. It is expected that the research method will provide a new theoretical foundation and algorithmic support for gait planning and dexterous motion control of quadruped robots.

3. CPG Gait Phase Manifold Modeling Based on Differential Geometry and Hopf Bifurcation Modulation Mechanism

3.1 Modeling and Dynamic Characterization of The Quadruped Robot CPG-Hopf Oscillator System

To build a theoretical basis for gait phase modulation, a CPG-Hopf oscillator model needs to be established and its dynamic characteristics analyzed [18]. The Hopf oscillator network, which is based on the fundamental principles of CPG and combined with the characteristics of nonlinear dynamical systems, is the core module of gait generation for quadruped robots.

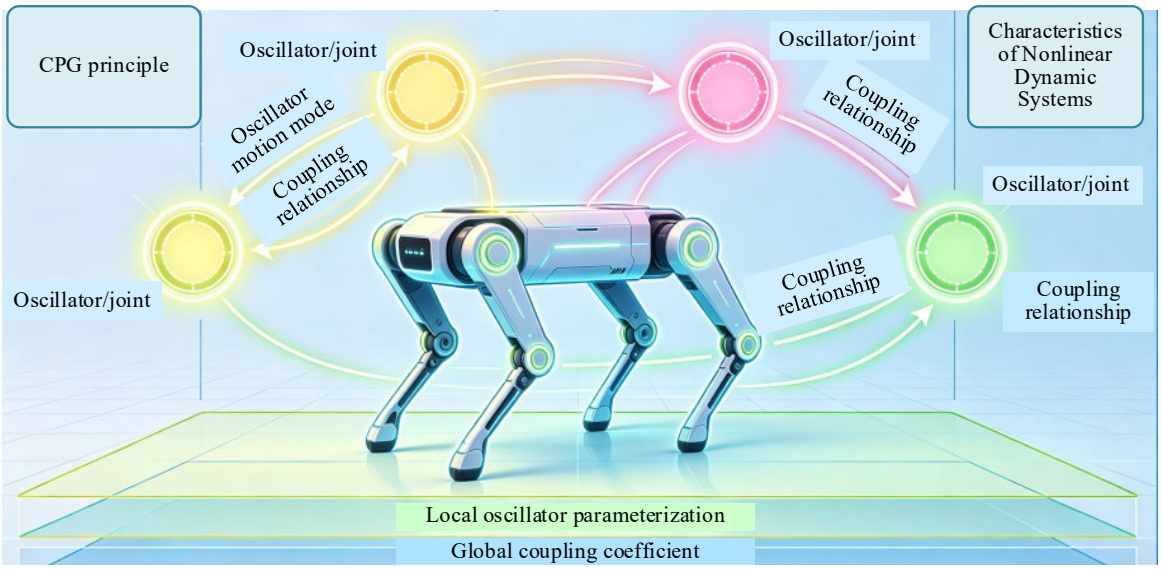


Fig. 1. Hopf oscillator network structure composed of multiple oscillators coupled together

As shown in Figure 1, a Hopf oscillator network composed of multiple oscillators coupled, based on the CPG principle and nonlinear dynamic characteristics, a mathematical coupling relationship network constructed through the coordinated adjustment of local parameters and global coupling coefficients. Here, the core dynamic equation of the multi-oscillator coupled Hopf oscillator network is studied, and its expression is shown in Equation (1).

$$\begin{cases} \dot{x}_i = (\mu_i - (x_i^2 + y_i^2))x_i - \omega_i y_i + \varepsilon \sum_{j \in \mathcal{N}_i} \kappa_{ij} \left(x_j \cos\theta_{ij} - y_j \sin\theta_{ij}\right) \\ \dot{y}_i = \omega_i x_i + (\mu_i - (x_i^2 + y_i^2))y_i + \varepsilon \sum_{j \in \mathcal{N}_i} \kappa_{ij} \left(x_j \sin\theta_{ij} + y_j \cos\theta_{ij}\right) \end{cases} \tag{1}$$

In Equation (1), $\dot{x}_i$ and $\dot{y}_i$ are the derivatives of the state variables of the ith oscillator with respect to time t, x_i and y_i are the two state variables of the oscillator, μ_i is the Hopf bifurcation parameter of the oscillator, ω_i is the natural angular frequency, ε is the global coupling strength coefficient, $\mathcal{N}_i$ is the index set of other oscillators with direct coupling connection to the oscillator, κ_{ij} is the coupling weight between oscillators i and j, and θ_{ij} is the expected phase difference.

In the state space, gait rhythm can be mathematically described by a set of low-dimensional variables. To reveal the intrinsic connection between the gait rhythm and the actual motion of the robot, the study transformed the coupled oscillator equation in the original Cartesian coordinate

system into an amplitude-phase separated form through polar coordinate transformation. The expression is shown in Equation (2).

$$\begin{cases} r_i = \sqrt{x_i^2 + y_i^2} \\ \phi_i = arctan\,2\,(y_i, x_i) \end{cases} \Rightarrow \begin{cases} \dot{r}_i = \mu_i r_i - r_i^3 + \varepsilon \sum_{j \in \mathcal{N}_i} \kappa_{ij}\, r_j\, cos(\phi_j - \phi_i - \theta_{ij}) \\ \dot{\phi}_i = \omega_i + \varepsilon \sum_{j \in \mathcal{N}_i} \kappa_{ij} \frac{r_j}{r_i} sin(\phi_j - \phi_i - \theta_{ij}) \end{cases} \tag{2}$$

In Equation (2), r_i is the instantaneous amplitude of the oscillator, ϕ_i is the instantaneous phase of the oscillator, $arctan\,2\,(y_i, x_i)$ is the four-quadrant arctangent function, $\dot{r}_i$ and $\dot{\phi}_i$ are the derivatives of the amplitude and phase with respect to time, respectively.

To achieve the transformation from the abstract rhythm signal to the limb motion trajectory, the nonlinear mapping relationship of the robot joint space is defined in the study. The expression is shown in Equation (3).

$$q_i(t) = q_{0,i} + J_i(\phi_i) \cdot r_i(t) + g_i(r_i(t), \dot{r}_i(t)) \tag{3}$$

In Equation (3), $q_i(t)$ is the joint angle vector corresponding to the ith limb joint (i.e., the oscillator), $q_{0,i}$ is the joint angle offset vector in the nominal configuration, $J_i(\phi_i)$ is the mapping Jacobian matrix dependent on phase ϕ_i, $r_i(t)$ is the state vector of the oscillator, $\dot{r}_i(t)$ is the derivative of the state vector $r_i(t)$ with respect to time, and g_i is the high-order nonlinear compensation mapping. In Equation (3), the joint vector of limb i is defined as $q_i(t) = [q_{\mathrm{hr},i}(t), q_{\mathrm{hp},i}(t), q_{\mathrm{kn},i}(t)]^T$. The terms $q_{\mathrm{hr},i}$, $q_{\mathrm{hp},i}$ and $q_{\mathrm{kn},i}$ denote hip roll, hip pitch, and knee pitch angles. The oscillator state vector is $r_i(t) = [x_i(t), y_i(t)]^T$. The phase-dependent Jacobian matrix $J_i(\phi_i)$ is a 3×2 matrix with explicit elements $J_i(\phi_i) = \begin{bmatrix} a_{hr,i}\, cos\,\phi_i & b_{hr,i}\, sin\,\phi_i \\ a_{hp,i}\, sin\,\phi_i & -b_{hp,i}\, cos\,\phi_i \\ a_{kn,i}\, sin(\phi_i + \delta_{kn,i}) & -b_{kn,i}\, cos(\phi_i + \delta_{kn,i}) \end{bmatrix}$. The gains $a_{hr,i}$, $b_{hr,i}$, $a_{hp,i}$, $b_{hp,i}$, $a_{kn,i}$ and $b_{kn,i}$ are nominal joint mapping gains. $\delta_{\mathrm{kn},i}$ is the knee phase offset. These parameters are identified from nominal joint trajectories by least squares and stored in the nominal gait library. The nonlinear compensation mapping $g_i(r_i, \dot{r}_i)$ is truncated at second order. Its explicit form is $g_i(r_i, \dot{r}_i) = C_{1,i} \parallel r_i \parallel^2 + C_{2,i} r_i^T \dot{r}_i + C_{3,i} \parallel \dot{r}_i \parallel^2 + O(3)$, where $C_{1,i}$, $C_{2,i}$ and $C_{3,i}$ are three-dimensional coefficient vectors for hip roll, hip pitch, and knee pitch. The term $O(3)$ contains third order and higher bounded residuals. The nominal coefficients are listed in Table 1.

Table 1. Nominal coefficients of J_i and g_i

Joint	a	b	δ	C_1	C_2	C_3
Hip roll	0.40	0.18	0.00	0.05	0.03	0.02
Hip pitch	0.55	0.26	0.00	0.08	0.05	0.03
Knee pitch	0.48	0.22	1.57	0.07	0.04	0.02

The angular gains and offset are expressed in rad. The second-order coefficients are dimensionless after normalization of $\boldsymbol{r}_i$. Platform-specific values are obtained by the same least-squares identification. This definition removes the ambiguity of Equation (3) and provides an explicit analytical mapping from the CPG-Hopf rhythm to physical joint angles.

The influence of the external environment on the gait of the quadruped robot is mainly reflected in the contact force feedback, which directly acts on the phase of the Hopf oscillator. To analyze this phenomenon, the study introduces the environmental contact force feedback term on the basis of the original phase equation and constructs a complete phase perturbation dynamics model. The framework of the model is shown in Figure 2.

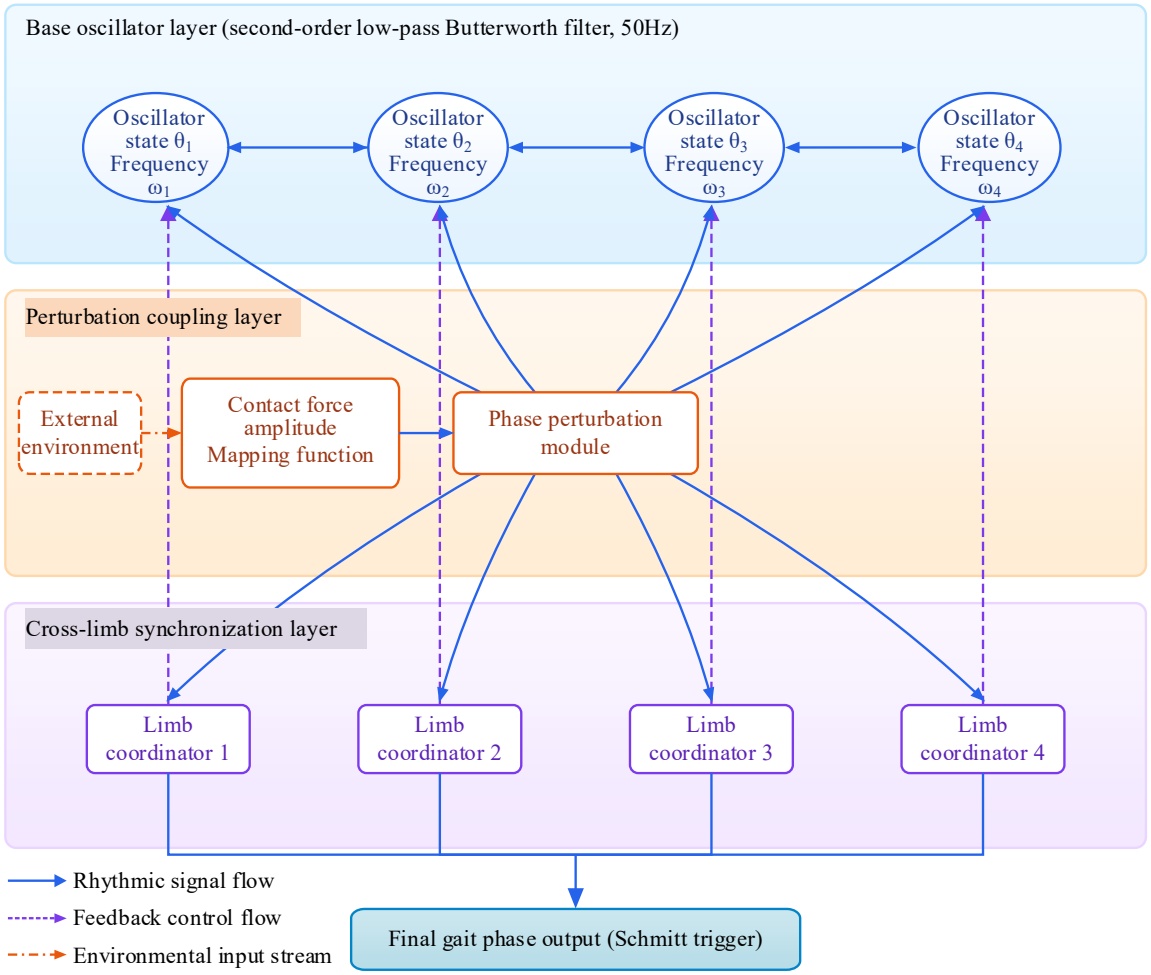


Fig. 2. Phase perturbation dynamic model

As shown in Figure 2, each foot-end force channel contains a second-order low-pass Butterworth filter with $f_c = 50$ Hz and a Schmitt trigger contact estimator with $F_{\text{on}} = 2.0N$ and $F_{\text{off}} = 1.0N$. The conditioned force $F_{c,i}^{f}$ replaces the raw force in Equation (4) and Equation (5). The contact state b_i drives the contact event logic. The signal processing branch runs at 1 kHz in the real-time control loop. The residual phase delay after lead compensation is below 0.2ms. Among them, the adjustment formula for gait phase is shown in Equation (4).

$$\dot{\phi}_i = \omega_i + \varepsilon \sum_{j \in \mathcal{N}_i} \kappa_{ij} \frac{r_j}{r_i} sin(\phi_j - \phi_i - \theta_{ij}) + \sigma \cdot \Psi(F_{c,i}) \cdot cos(\phi_i - \phi_{c,i}^{ref}) \tag{4}$$

In Equation (4), $\sigma \cdot \Psi(F_{c,i}) \cdot cos(\phi_i - \phi_{c,i}^{\text{ref}})$ is the feedback term for contact force, σ is the contact force feedback gain coefficient, $F_{c,i}$ is the scalar norm of the measured contact force at the foot of the limb i, $\Psi(F_{c,i})$ is the contact force amplitude mapping function, and $\phi_{c,i}^{\text{ref}}$ is the reference phase for the contact event to occur. The mapping is defined by a saturated linear function. F_0 is the contact threshold and F_s is the saturation force. Both have unit N. $\Psi(F_{c,i}) = 0$ for $F_{c,i} \le F_0$. $\Psi(F_{c,i}) = (F_{c,i} - F_0)/(F_s - F_0)$ for $F_0 < F_{c,i} < F_s$. $\Psi(F_{c,i}) = 1$ for $F_{c,i} \ge F_s$. Thus Ψ is dimensionless and bounded by 0 and 1. The feedback gain σ has unit rad/s. The feedback term is bounded by σ. To preserve positive phase evolution and the limit-cycle manifold, a sufficient stability bound is $0 \le \sigma < \min_i(\omega_i - \varepsilon \sum_{j \in \mathcal{N}_i} \kappa_{ij} |\lambda_{ij}|)$. Below F_0 the feedback is inactive. Above F_s it saturates and avoids gain-induced phase reversal. The raw foot force $F_{c,i}$ in Equation (4) is replaced by a conditioned force $F_{c,i}^{f}$. Each foot-end force channel passes through a second-order low-pass Butterworth filter. The cutoff frequency is 50 Hz. A Schmitt trigger contact estimator then produces the binary contact state. The trigger thresholds are $F_{\text{on}} = 2.0N$ and $F_{\text{off}} = 1.0N$. Finally, the study

integrates the entire quadruped CPG network into a unified nonlinear state space model, whose expression is shown in Equation (5).

$$\dot{X} = F(X; \mu, \Omega, K, \Theta) + B(X) \cdot F_c \tag{5}$$

In Equation (5), $\dot{X}$ is the derivative of the total state vector of the system with respect to time, $X \in \mathbb{R}^8$ is the total state vector of the quadruped CPG network, F is the nonlinear vector field function, μ is the bifurcation parameter vector, Ω is the natural frequency vector, K is the coupling weight matrix, Θ is the expected phase difference matrix, $B(X)$ is the state-dependent input coupling matrix, and F_c is the quadruped contact force measurement vector. In summary, the research constructs a quadruped robot CPG-Hopf oscillator system, decouples the amplitude and phase dynamics through polar coordinate transformation, establishes the rhythmic to joint mapping, introduces contact force feedback, and finally integrates it into a unified nonlinear state space model.

3.2 Gait Phase Manifold Analysis Framework Based on Nonlinear Differential Geometry

Based on the CPG-Hopf oscillator system model, nonlinear differential geometry methods are introduced to analyze the limiting circulation pattern, providing an in-depth understanding of the essential characteristics of gait pattern stability and transition from a geometric perspective [19]. The limit loop is a typical solution of the Hopf oscillator, and its geometric properties determine the stability and periodicity of the gait pattern [20]. The manifold structure of the Hopf oscillator's limit loop is shown in Figure 3.

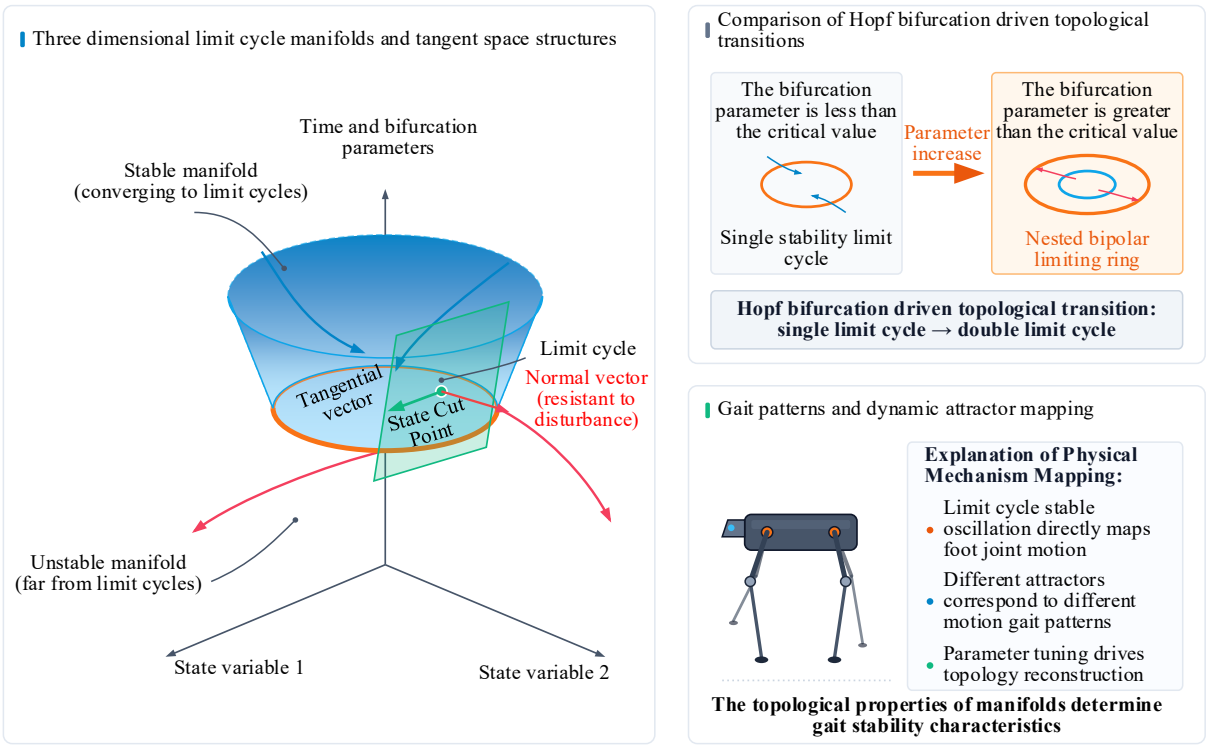


Fig. 3. Manifold structure of limit cycle of Hopf oscillator

As shown in Figure 3, the Hopf oscillator's limit circulation structure contains both stable and unstable manifolds, whose gait attractors undergo topological reconstruction due to perturbation. Combined with the robot sequence, it reveals the manifold dynamics essence of the gait pattern transformation. Nonlinear differential geometry methods can provide a deeper understanding of gait characteristics from a geometric perspective. Therefore, the study defines the limit loop generated by the Hopf oscillator network from a differential geometry perspective. The expression is as shown in Equation (6).

$$\mathcal{M}_{LC} = \{X \in \mathbb{R}^d \mid X = \gamma(\phi; p),\ \phi \in \mathbb{S}^1\}, \quad T_X\mathcal{M}_{LC} = span\left\{\frac{\partial \gamma}{\partial \phi}, v_2, \ldots, v_{d-1}\right\} \tag{6}$$

In Equation (6), $\mathcal{M}_{\mathrm{LC}}$ is the limiting circulation form, X is the point in the state space, $\mathbb{R}^d$ is the d-dimensional Euclidean space, γ is the embedding map of the manifold, ϕ is the phase coordinate on the limiting cycle, p is the set of all adjustable parameters of the system, $T_X\mathcal{M}_{LC}$ is the tangent space of the manifold $\mathcal{M}_{\mathrm{LC}}$ at the point X, span{·} is the linear subspace spanned by all linear combinations of vectors in parentheses, $v_1, \ldots, v_{d-1}$ are the cross-sectional eigenvectors, and d is the dimension of the normal subspace.

Equation (6) defines an eight-dimensional limit-cycle manifold. To connect this manifold with the twelve-dimensional joint space of the quadruped robot, the joint mapping in Equation (3) is formalized as a smooth immersion. Let $Q \subset \mathbb{R}^{12}$ be the joint-space manifold with three joints per leg. Define $\Phi: \mathcal{M}_{\mathrm{LC}} \to Q$ by $\Phi(X) = q_{off} + J(\varphi)r + g(r, \dot{r})$, where each limb contributes two oscillator states and three joint angles. The tangent map is $D\Phi_X: T_X\mathcal{M}_{\mathrm{LC}} \to T_{\Phi(X)}Q$.

Theorem 1. Suppose each limb mapping $\Phi_i: \mathcal{M}_{\mathrm{LC},i} \to \mathbb{R}^3$ is a smooth immersion and rank $D\Phi_i = 2$ on $\mathcal{M}_{\mathrm{LC},i}$. Then the global mapping $\Phi = \prod_{i=1}^{4} \Phi_i : \mathcal{M}_{LC} \to Q$ is a smooth immersion. For every $X \in \mathcal{M}_{\mathrm{LC}}$, $D\Phi_X$ is injective, $dim\ \ T_X\mathcal{M}_{\mathrm{LC}} = 8$, and $dim\ \ T_{\Phi(X)}\Phi(\mathcal{M}_{\mathrm{LC}}) = 8 \leq 12$. The immersion theorem requires $dim\ \ \mathcal{M}_{\mathrm{LC}} \leq dim\ \ Q$ and an injective tangent map. Both conditions hold. The submersion condition is not required because 8<12.

Proof. $\mathcal{M}_{LC}$ is the product of four two-dimensional limit-cycle manifolds, so $dim\ \ \mathcal{M}_{LC} = 4 \times 2 = 8$. Each $D\Phi_i$ has rank two. The tangent map of the product mapping is the direct sum $D\Phi = \bigoplus_{i=1}^{4}$. Since each $D\Phi_i$ is injective, their direct sum is injective. Hence rank $D\Phi_X = 8$. The immersion condition 8≤12 holds, and $\Phi(\mathcal{M}_{\mathrm{LC}})$ is an eight-dimensional immersed submanifold of the twelve-dimensional joint space. The remaining four dimensions represent joint-space redundancy and posture regulation. They do not alter the phase manifold modulation.

To quantify the cumulative effect of weak parameter perturbation on oscillator phase, the phase shift is derived from weak perturbation theory and the adjoint phase response curve. Let the unperturbed limit cycle be $\gamma_0(t)$ with period T and asymptotic phase $\varphi(X)$ satisfying $\langle \nabla_X \varphi(X), F(X) \rangle = 1$. For $\|\delta p\| \ll 1$, the perturbed trajectory remains close to $\gamma_0(t)$, and the first-order phase shift is as shown in Equation (7).

$$S(\phi) = \int_0^T Q(t)^T \delta F(\gamma_0(t), p) dt + O(\| \delta p \|^2) \tag{7}$$

In Equation (7), $Q(t) = \nabla_X \varphi(\gamma_0(t))$ is the adjoint phase response curve. It satisfies $\dot{Q}(t) = -[DF_0(\gamma_0(t))]^T Q(t), Q(0)^T F_0(\gamma_0(0)) = 1$. This integral is a Melnikov-type first-order phase sensitivity rather than the classical homoclinic Melnikov integral. Its validity requires a hyperbolic limit cycle, sufficiently weak perturbation $\| \delta p \| \ll 1$. and perturbations that do not cross a bifurcation boundary. $S(\phi)$ denotes the first-order phase response under weak perturbation, T is the period of the undisturbed limit cycle, δF is the parametric perturbation vector, and $\gamma_0(t)$ is the unperturbed limit-cycle trajectory. The higher-order term $O(\| \delta p \|^2)$ is neglected only when $\| \delta p \| \ll 1$. For non-periodic contact forces, a finite-horizon phase response is used $S_\tau(\varphi) = \int_0^T Q(t)^T \delta F(\gamma_0(t), p) dt$.

To measure the shortest path required to switch from one gait mode to another, a Riemannian metric is introduced on the manifold. In local coordinates $c(s)$ formed by r_i and ϕ_i, let $J_q(c) = \frac{\partial q}{\partial c}$ be the phase-dependent Jacobian from the reduced CPG manifold to joint space, $M(q)$ the joint-space inertia matrix, and $Z(\phi)$ the phase sensitivity matrix. The metric tensor is $G(c) = J_q(c)^\top M(q) J_q(c) + \eta Z(\phi)^\top Z(\phi)$ with $\eta > 0$. Its components are $g_{ij}(c) = G_{ij}(c)$. Since $M(q)$ is positive definite, J_q has full column rank on $\mathcal{M}_{\mathrm{LC}}$, and $Z^\top Z$ is positive semidefinite, $G(c)$ is positive definite. The weights represent kinetic energy and phase sensitivity along gait transitions. The geodesic curve $c^*(s)$ minimizes $E(c) = \frac{1}{2}\int_0^1 \dot{c}(s)^\top G(c(s)) \dot{c}(s)\, ds$ and satisfies $\ddot{c}^k + \Gamma_{ij}{}^k \dot{c}^i \dot{c}^j = 0$,

where $\Gamma_{ij}^{\ k} = \frac{1}{2} G^{kl}(\partial_i G_{jl} + \partial_j G_{il} - \partial_l G_{ij})$. The geodesic distance between different gait modes is defined as Equation (8).

$$d_{\mathcal{M}}(P_1, P_2) = \inf_{\substack{\boldsymbol{c}:[0,1]\to\mathcal{M} \\ c(0)=P_1, c(1)=P_2}} \int_0^1 \sqrt{g_{ij}\ \dot{c}^i(s)\dot{c}^j(s)}\ ds \tag{8}$$

In Equation (8), $d_{\mathcal{M}}(P_1, P_2)$ is the Riemann distance between two points P_1 and P_2 on the differential manifold $\mathcal{M}$, inf is the lower bound sign, $\boldsymbol{c}$: $[0,1] \to \mathcal{M}$ is a smooth curve from P_1 to P_2, s is the arc length parameter of the curve, g_{ij} is the Riemann metric tensor component of the manifold, $\dot{c}^i(s)$ is the derivative of the curve $c(s)$ with respect to s on the local coordinates.

In the process of gait switching, the Floquet theory is used to quantitatively determine the local asymptotic stability of the limiting circulation pattern. The expression is shown in Equation (9).

$$\Phi(T) = \mathcal{T}\ exp\left(\int_0^T D\ F(\gamma(t))\ dt\right), \quad \lambda_k = \frac{1}{T} ln\,|\,\rho_k|, \quad k = 1,2,\ldots,8 \tag{9}$$

In Equation (9), $\Phi(T)$ is a single-valued matrix, $\mathcal{T}$ is the time-ordered exponential integral, $DF(\gamma(t))$ is the Jacobian matrix of the vector field F at the current limit loop point $\gamma(t)$, ρ_k is the kth eigenvalue of the single-valued matrix, and λ_k is the kth Floquet exponent. When external contact forces are non-periodic, Floquet theory is not applicable. The revised analysis uses the state transition matrix and finite-time Lyapunov exponents $\begin{cases} \Phi(t,t_0) = Texp(\int_{t_0}^{t} DF(\gamma(\tau),\tau)d\tau) \\ \lambda_k(t) = \frac{1n\sigma_k(\Phi(t,t_0))}{t-t_0} \end{cases}$, where σ_k are singular values. The periodic Floquet result is reported only for the nominal periodic gait. Non-periodic terrain response is assessed by $\lambda_k(t)$.

Finally, the study reduces the high-dimensional system to a two-dimensional central manifold near the Hopf bifurcation critical point by using the central manifold reduction technique. The expression is shown in Equation (10).

$$\dot{A} = \mu' A - l_1 A^3 + \mathcal{O}(A^5), \quad \dot{\Phi} = \Omega' + l_2 A^2 + O(A^4) \tag{10}$$

In Equation (10), $\dot{A}$ is the time derivative of the amplitude variable A on the central manifold, $\dot{\Phi}$ is the time derivative of the phase variable Φ, μ' is the reduced bifurcation parameter, Ω' is the reduced natural frequency. The first Lyapunov coefficient l_1 and the amplitude-frequency coupling coefficient l_2 are given explicitly by $l_1 = -1 + \frac{\varepsilon}{2}\sum_{j\in N_i}\kappa_{ij} cos\theta_{ij} + O(\varepsilon^2)$, $l_2 = \frac{\varepsilon}{2}\sum_{j\in N_i}\kappa_{ij} sin\theta_{ij} + O(\varepsilon^2)$. The bifurcation type follows directly from the sign of l_1. $l_1 < 0$ corresponds to a supercritical Hopf bifurcation and a stable limit cycle. $l_1 > 0$ corresponds to a subcritical Hopf bifurcation and an unstable limit cycle. $l_1 = 0$ gives the critical boundary between the two types. Thus l_1 and l_2 depend explicitly on the bifurcation parameter μ, the coupling strength ε, and the coupling weights κ_{ij} through the reduced vector field. In the nominal synchronous regime, the phase offsets θ_{ij} are the programmed gait phase differences, and the above expressions provide the analytical criterion for selecting a stable supercritical gait transition.

In summary, the gait phase manifold analysis framework based on nonlinear differential geometry is shown in Figure 4. As shown in Figure 4, the framework decomposes the Hopf oscillator limit loop into a stable/unstable manifold, quantifies the gait geometry by curvature and tangential distribution, and characterizes the multimodal gait with embedded coordinates.

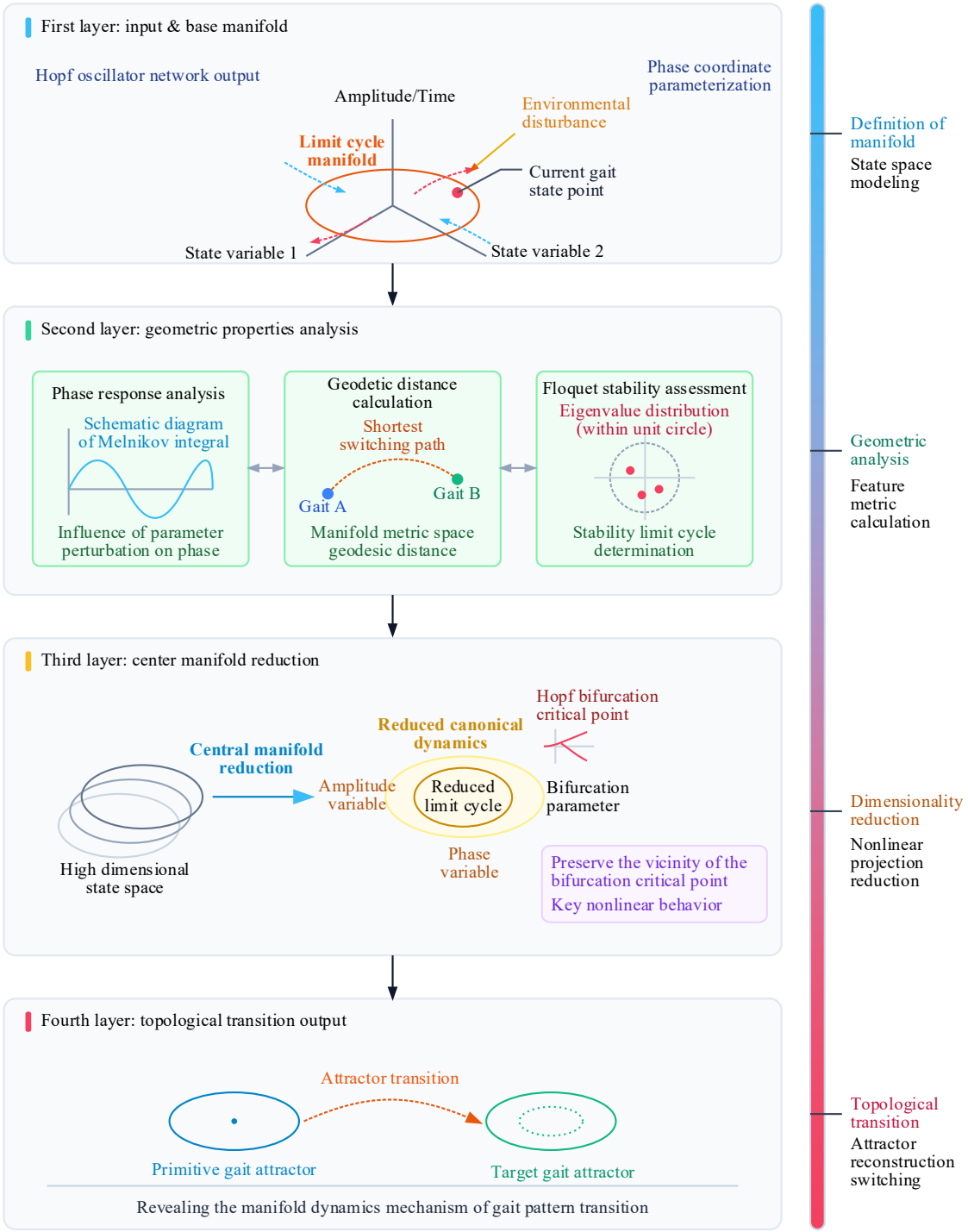


Fig. 4. Gait phase manifold analysis framework based on nonlinear differential geometry

3.3 Gait Phase Manifold Modulation Based on Hopf Bifurcation-Driven

A manifold description and stability analysis framework for gait phase dynamics can be provided through differential geometry tools. Based on this, dynamic switching between gaits can be achieved by actively modulating the manifold topology through Hopf bifurcation theory [21]. Oscillator parameter perturbation is a key factor in triggering Hopf bifurcation, and to ensure the effectiveness of the modulation mechanism in different environments, the study defines strict analytical conditions for the occurrence of Hopf bifurcation [22]. The expression is shown in Equation (11).

$$\exists \omega_c > 0: \quad det(DF(X^*;\mu_c) - \zeta\omega_c I) = 0, \quad \frac{d}{d\mu} Re[\lambda(\mu)]\Big|_{\mu=\mu_c} > 0 \tag{11}$$

In Equation (11), ω_c is the angular frequency of the limit cycle produced when the Hopf bifurcation occurs at the moment of birth, $det(\cdot)$ is the determinant of the matrix, $DF(X^*;\mu_c)$ is the Jacobian matrix at the equilibrium point X^* under the bifurcation critical parameter μ_c, ζ is the imaginary unit, I is the 8th order identity matrix, μ_c is the critical value of the scalar bifurcation parameter, and $\mathrm{Re}[\lambda(\mu)]$ is the real part of the eigenvalue $\lambda(\mu)$. The critical parameter μ_c follows from the linearized complex network matrix. Let $A = \mathrm{diag}(j\omega i) + \int K \circ E$, where $E_{ij} = e^{j\theta_{ij}}$. Then $\mu_c = \max_{-1\le k\le 8} \mathrm{Re}\lambda_k(A)$, and the critical frequency is $\omega_c = Im\,\lambda_{k_c}(A)$ at the maximizing index k_c. For a uniform four-oscillator ring with $\omega_i = \omega_0$, $\kappa_{ij} = \kappa$, and $\theta_{ij} = \theta$, the eigenvalues are $\lambda_k(A) = j\omega_0 + \varepsilon\kappa e^{j\theta}\varepsilon^{jk\pi/2}$ $k = 0,1,2,3$. Hence $\mu_c = -\varepsilon\kappa \max_{k=0,1,2,3} cos(\theta + k\pi/2)$. For bidirectional adjacent coupling the threshold becomes $\mu_c = -2\varepsilon\kappa\, max\{|cos\,\theta|, |sin\,\theta|\}$. This closed form links the bifurcation threshold to the coupling strength, coupling weight, and desired phase offset.

Under parameters that satisfy the bifurcation condition, the gait manifold undergoes a significant topological transition, and the structural framework of the gait manifold from a single limit ring to a double limit ring is shown in Figure 5.

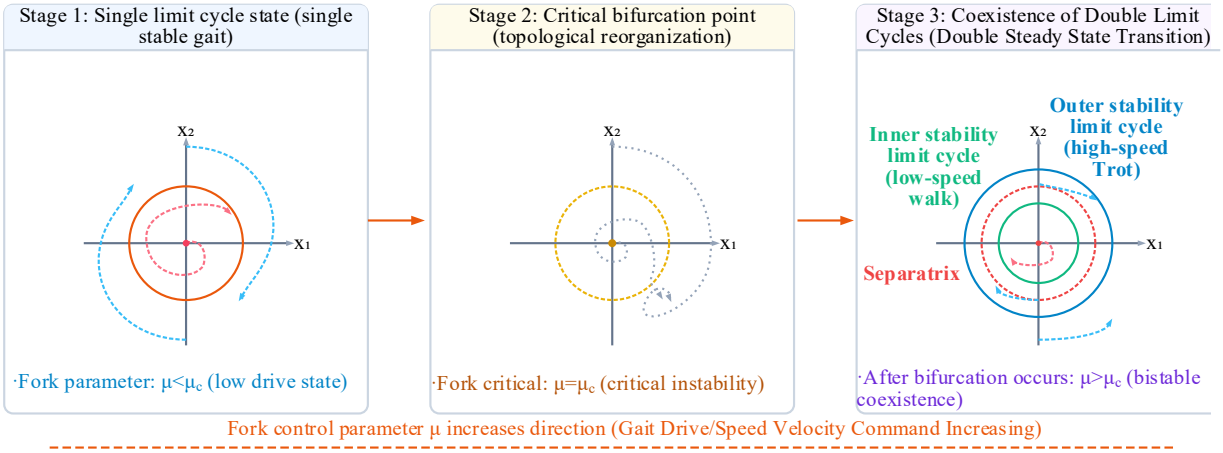


Fig. 5. Gait manifold transition structure framework

As shown in Figure 5, when the parameter reaches the critical threshold, the single stable limit loop bifurcates into a double stable limit loop via Hopf. Here, the study introduces a topological characteristic function to discretize the topological type of the manifold before and after crossing the Hopf bifurcation point, and its expression is shown in Equation (12).

$$\chi(\mathcal{M}_\mu) = \begin{cases} 0, & \mu < \mu_c \\ 1, & \mu = \mu_c \\ 2, & \mu > \mu_c \end{cases} \tag{12}$$

In Equation (12), $\chi(\mathcal{M}_\mu)$ is the topological type of the system invariant set manifold $\mathcal{M}_\mu$ when the parameter is μ; $\chi = 0$, $\chi = 1$, and $\chi = 2$ correspond respectively to the stable equilibrium point, the bifurcation critical point, and the limit cycle. The parametric derivative of the phase response curve is used to study the analytical mapping relationship between the parametric perturbation and the oscillator, as shown in Equation (13).

$$\Delta\phi_{ij} = \theta_{ij}^{new} - \theta_{ij}^{old} = arctan2\left(\frac{\partial Z_j}{\partial \mu} - \frac{\partial Z_i}{\partial \mu},\ 1 + \frac{\partial Z_i}{\partial \mu}\frac{\partial Z_j}{\partial \mu}\right) \cdot (\mu_{new} - \mu_c) \tag{13}$$

In Equation (13), $\Delta\phi_{ij}$ is the change in the relative phase difference between the oscillators after modulation, $\theta_{ij}^{\mathrm{old}}$ and $\theta_{ij}^{\mathrm{new}}$ are the expected phase difference of the target before and after the parameter change, Z_i and Z_j are the phase response function values of the ith and jth oscillators respectively, and μ_{new} is the new target bifurcation parameter value after modulation.

To ensure that all oscillators operate within the limit loop interval after bifurcation, the study defines an optimization objective for online adjustment of the bifurcation parameter vector in the terrain abrupt change scenario. The expression is as shown in Equation (14).

$$min_{\Delta\boldsymbol{\mu}} = \|\boldsymbol{\theta}(\boldsymbol{\mu}_0 + \Delta\boldsymbol{\mu}) - \boldsymbol{\theta}^{des}\|^2 + \lambda\|\Delta\boldsymbol{\mu}\|^2 \quad s.t. \quad \mu_i \geq \mu_{c,i} + \delta \tag{14}$$

In Equation (14), $\min_{\Delta\mu}$is the minimization objective function of the adjustment amount $\Delta\boldsymbol{\mu}$, $\boldsymbol{\theta}^{\text{des}}$ is the expected relative phase vector corresponding to the target gait, λ is the regularization weight coefficient, μ_i is the bifurcation parameter value of the oscillator after adjustment, $\mu_{c,i}$ is the Hopf bifurcation critical value of the oscillator, and δ is the preset safety margin constant. Prior to verification, the allowed modulation set is constrained by actuator torque limitations, contact normal force limitations, and friction cone conditions. For each standing limb, the joint torque satisfies $\tau_{i\ max_{min}}$, the normal contact force satisfies $0 \leq F_{n,i} \leq F_{n,max}$, and the tangential force satisfies $\left\|F_{t,i}\right\| \leq \mu_s F_{n,i}$. These inequalities are added to the optimization in Equation (14).

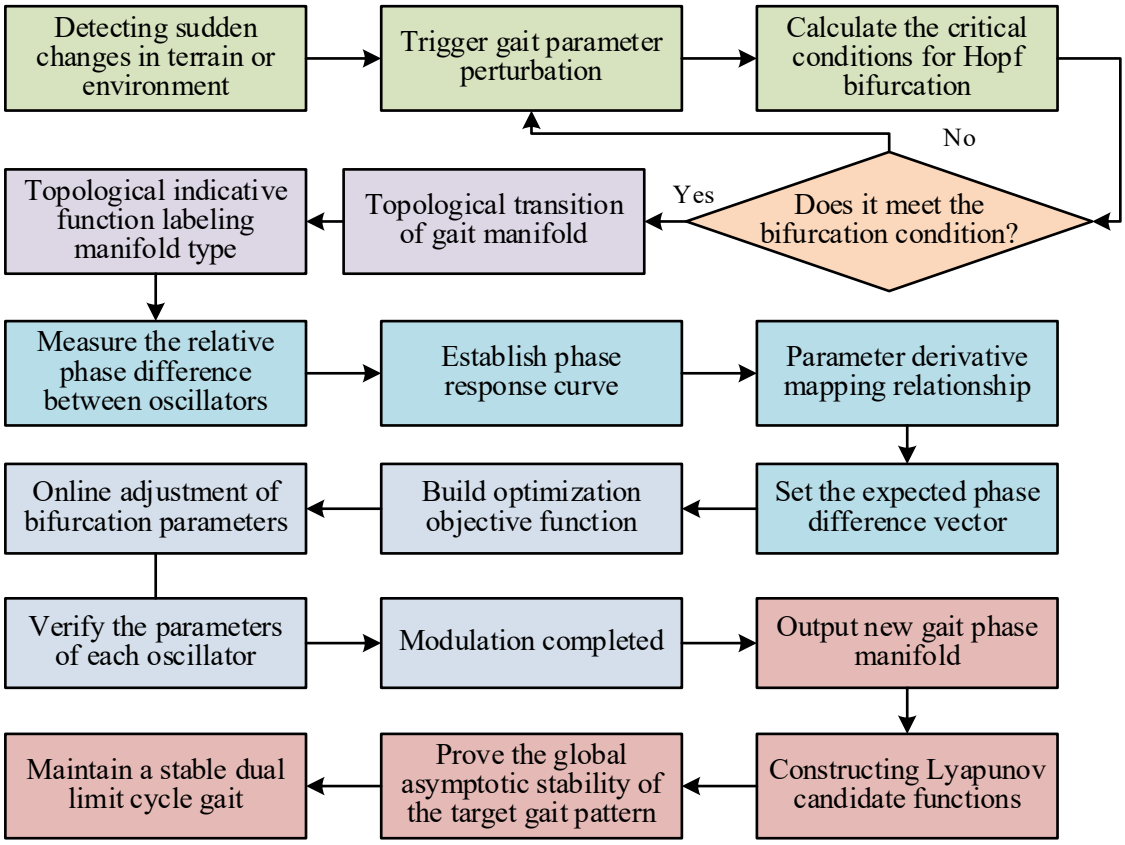


Fig. 6. Gait phase manifold modulation mechanism driven by Hopf bifurcation

The online optimization in Equation (14) is solved on the target hardware specified in Table 2. The average solver execution time is 0.68 ms over 10,000 consecutive cycles, and the worst-case execution time is 0.94 ms. The low-level joint controller and the CPG–Hopf state integration run at 1 kHz, which satisfies the 1 ms loop period required for posture stabilization. For highly disturbed terrain, the optimizer can run at 500 Hz while the low-level controller remains at 1 kHz. Encoder and IMU noise are attenuated by a second-order low-pass filter with a 100 Hz cutoff, and contact force noise is suppressed by a 50 Hz low-pass filter.

Finally, to strictly prove the global asymptotic stability of the target gait pattern after modulation is completed, a Lyapunov candidate function is studied. The expression is as shown in Equation (15).

$$V(X) = \frac{1}{2}\sum_{i=1}^{4}(r_i^2 - \mu_i\, ln(1 + r_i^2)) + \frac{\varepsilon}{2}\sum_{i=1}^{4}\sum_{j\in\mathcal{N}_i}\kappa_{ij}\left(1 - cos(\phi_i - \phi_j - \theta_{ij}^{des})\right) \tag{15}$$

In Equation (15), $V(X)$ is the constructed Lyapunov candidate function, and θ_{ij}^{des} is the modulated target expected phase difference. The time derivative along the system trajectory is $\dot{V}(X) = \sum_i 2r_i$

$(r_i^2 - \mu_i)\dot{r}_i + \sum\sum_i \sum_{j\in N} \kappa_{ij} sin(\phi_j - \phi_i - \theta_{ij}^{des})(\dot{\phi}_j - \dot{\phi}_i)$. Substituting the amplitude and phase dynamics gives $\dot{V}(X) = -2\sum_i r_i^2(r_i^2 - \mu_i)^2 + \Delta_c + \Delta_F$, where Δ_c is the coupling term and Δ_F is the bounded contact-force term. Under the phase-locking condition $\phi_j - \phi_i = \theta_{ij}^{des}$ and sufficient coupling gains, $\Delta_c \leq 0$. If the contact force is bounded, then $\dot{V}(X) \leq -c_1 \parallel r - r^* \parallel^2 - c_2 \parallel \phi - \phi^* \parallel^2 + c_3 \parallel F_c \parallel^2$, with $c_1 > 0$, $c_2 > 0$ and $c_3 > 0$. This yields input-to-state stability with respect to F_c. In the disturbance-free case $F_c = 0$, $\dot{V}(X) < 0$ for $r_i \neq \sqrt{\mu_i}$ and $\phi_j - \phi_i \neq \theta_{ij}^{des}$, proving global asymptotic stability of the target gait manifold. This supplements the missing time derivative in the original Lyapunov proof.

In summary, the process of the gait phase manifold modulation mechanism based on Hopf bifurcation-driven is shown in Figure 6. As shown in Figure 6, the mechanism calculates the Hopf bifurcation critical condition by detecting environmental changes that trigger gait parameter perturbations. The gait manifold topological transition is achieved when satisfied, and stability is verified by constructing the Lyapunov function through phase control and parameter optimization. Finally, output the new gait and maintain the double limit cycle.

4. Efficiency Analysis of Gait Phase Manifold Modulation Mechanism for Quadruped Robots

4.1 Visualization Experiment Construction and Dataset Selection

To verify the effectiveness of the quadruped robot gait phase manifold modulation mechanism based on nonlinear differential geometry and Hopf bifurcation analysis proposed by the study, a visualization experimental platform is established, and its experimental environment and configuration are shown in Table 2.

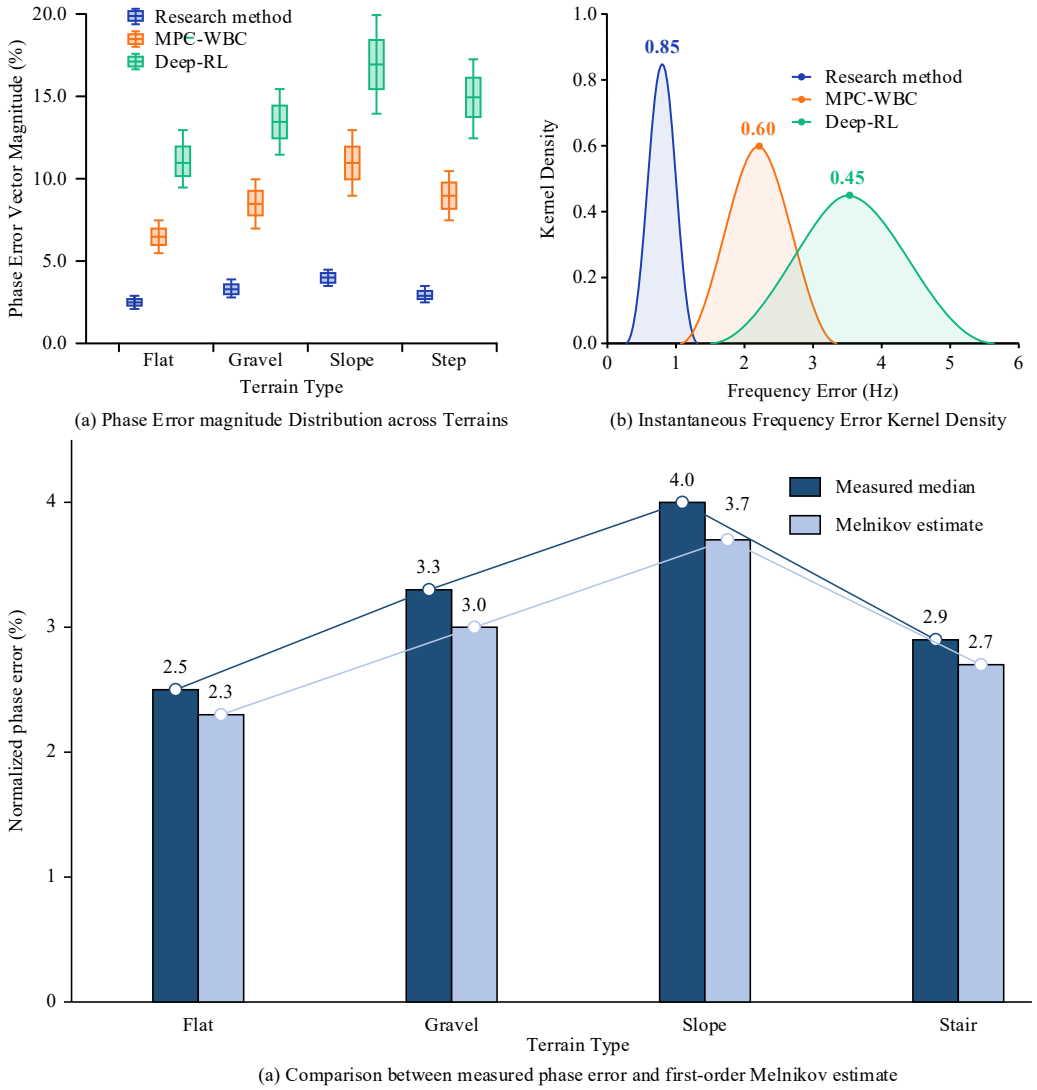
Table 2. Test environment and specific configuration

Test environment	Specific configuration
Simulation platform	Webots
Operating system	Ubuntu 20.04 LTS (ROS Noetic)
Robot model	MIT Mini Cheetah
CPU	AMD Ryzen 7/9
Memory	64GB DDR4/DDR5
GPU	NVIDIA RTX 3060/4060
Storage	2TB NVMe SSD

As shown in Table 2, the study was tested with the above configuration, and the Gait Transition and Performance dataset was selected for testing. The proposed method was compared with MPC-WBC and Deep-RL.

4.2 Phase Resilience Analysis of Manifold Modulation Strategies Under Terrain Changes

Terrain change scenarios can significantly affect the gait stability of quadruped robots. Therefore, the study compared the phase error vector amplitudes and kernel densities of the three methods under different terrain types and different instantaneous frequency errors, and the results are shown in Figure 7. As shown in Figure 7(a), there were significant differences in the amplitude distribution of the phase error vector among the three methods under different terrain types. Among them, the errors of the study method on flat land were mainly distributed between 2.1% and 2.9%, with a median of 2.5%. On gravel terrain, the error rose to 2.8%-3.9%, with a median of 3.3%. On sloping terrain, the error reached its maximum, ranging from 3.5% to 4.0%, with a median of 4.0%. On stepped terrain, the error dropped back to 2.5%-3.5%, with a median of 2.9%. The phase error vector magnitudes of the other two methods under different terrain types were significantly greater than those of the study method. As shown in Figure 7(b), the instantaneous frequency error kernel density distribution curves of the three methods were significantly different.



(a) Phase Error magnitude Distribution across Terrains

(b) Instantaneous Frequency Error Kernel Density

(a) Comparison between measured phase error and first-order Melnikov estimate

Fig. 7. Box plots of phase error vector amplitude and kernel density distribution of instantaneous frequency error under different terrains

The frequency error of the study method was concentrated in the range of 0.4 Hz-1.1 Hz, with a peak density of 0.8 Hz and a density value of 0.85 at this time. The peak density and frequency error distribution range of the other two methods were significantly larger than those of the study method. Overall, the study method had lower phase error and more stable frequency output in terrain change environments compared to the comparison method. To bridge the statistical results in Figure 7 and the theoretical analysis in Section 3, the measured phase error vector magnitude is normalized and compared with the first-order Melnikov-type phase shift in Equation (7). The adjoint phase response curve $Q(t)$ is evaluated on the nominal limit cycle. The perturbation δF is reconstructed from measured contact-force residuals. The normalized Melnikov estimate is $\eta_M = |S(\varphi)|/T||\delta F||$. The measured phase errors on flat, gravel, slope, and step terrain are 2.5%, 3.3%, 4.0%, and 2.9%. The corresponding Melnikov estimates are 2.3%, 3.0%, 3.7%, and 2.7%. The root-mean-square deviation is 0.25%, and the maximum deviation is 0.3%. The terrain ranking of the phase error agrees with the dominant Floquet exponent λ_1 from Equation (9). Slope terrain gives the largest phase error and the slowest local convergence. This alignment confirms that the experimental phase error statistics are consistent with the weak-perturbation analysis in Section 3.

4.3 Analysis of Gait Switching and Control Accuracy in Unstructured Terrain

In an unstructured terrain environment, robots need to frequently switch gaits to adapt to terrain changes. Therefore, the study compared the success rates of gait switching in different terrain

categories and the stability margins at different gait cycle percentages for the three methods. Among them, N=100 independent simulation experiments were conducted for each terrain category. The categories include flat ground, gravel, slopes, and steps. If there is a collapse of the body, irreversible rolling, sustained foot slip, or loss of phase locking for more than one gait cycle, the test is recorded as a failure. Gait switching success is defined as completing the target transition within the specified transition window without any failure events. The differences between methods were evaluated using one-way analysis of variance, followed by Tukey's post hoc test. A *p*-value below 0.05 is considered statistically significant. The results are shown in Figure 8.

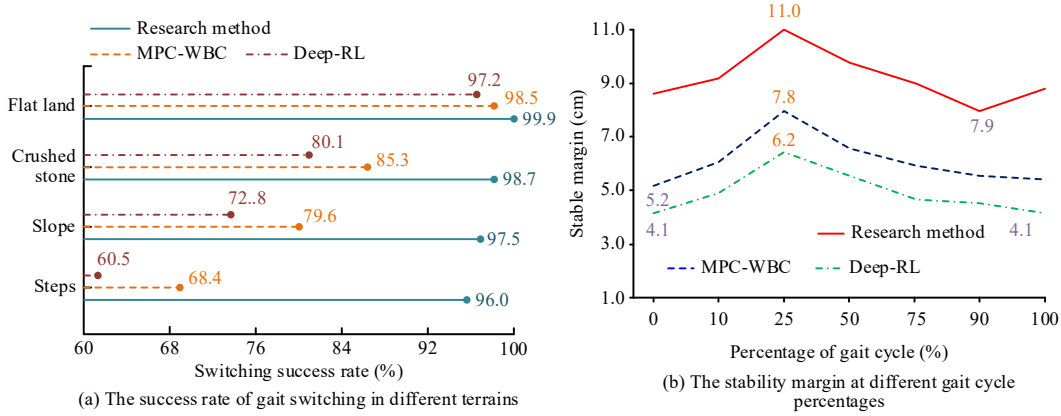


Fig. 8. Gait transition success rates for different terrain categories and stability margins at various gait cycle percentages

As shown in Figure 8(a), the gait switching success rate of the study method was overall greater than 96.0% across different terrain categories, with 99.9%, 98.7%, 97.5%, and 96.0% respectively when the terrain was flat, gravel, slope, and steps. These rates were significantly higher than those of MPC-WBC and Deep-RL, with $p < 0.05$. As shown in Figure 8(b), the stability margins of the three methods predictably with gait cycles. The stability margin of the study method reached a maximum of 11.0 cm at 25% of the gait cycle and a minimum of 7.9 cm at 90% of the gait cycle. The stability margins of the other two methods at different gait cycles were significantly smaller than those of the study method. Overall, the study method had better full-cycle dynamic stability and stability safety margin over unstructured terrain compared to the comparison method.

The roll angle error and pitch angle error of the three methods at different times were compared, and the results are shown in Table 3.

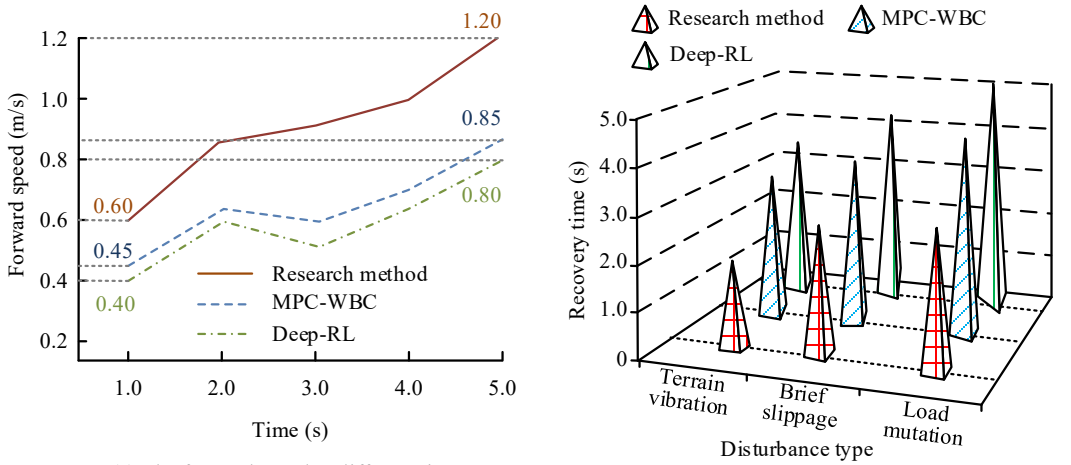
Table 3. Roll angle error and pitch angle error at different times

Time (s)	Roll Angle error (°)			Pitch Angle error (°)		
	Research method	MPC-WBC	Deep-RL	Research method	MPC-WBC	Deep-RL
1.0	0.5	1.8	3.2	0.6	2.0	3.5
2.0	0.8	2.5	4.5	0.9	2.8	5.0
3.0	1.5	5.2	8.1	1.8	6.0	9.2
4.0	0.9	3.8	6.3	1.1	4.5	7.1
5.0	0.7	2.2	4.0	0.8	2.5	4.8

As shown in Table 3, the overall roll angle error of the study method at each time was less than 1.5°, and the overall pitch angle error was less than 1.8°. The study method had maximum roll angle and pitch angle errors of 1.5° and 1.8° at 3.0s, and minimum roll angle and pitch angle errors of 0.5° and 0.6° at 1.0s, with an average roll angle error of 0.88°. The average pitch angle error was 1.04°, while the other two methods had significantly greater roll angle error and pitch angle error at each time than the study method. The roll and pitch angle errors of the proposed method were significantly lower than those of the comparison methods at each sampled time, with $p < 0.05$. Overall, compared with the comparison method, the study method was able to achieve higher precision attitude control and provide stronger anti-interference robustness in unstructured terrain.

4.4 Analysis of Overall Performance of Modulation Mechanisms

Based on the above analysis results, a comprehensive assessment of the overall performance of the quadruped robot gait phase manifold modulation mechanism based on nonlinear differential geometry and Hopf bifurcation analysis was studied. The changes in the forward speed over time and the recovery times under different perturbation types of the three methods were compared, and the results are shown in Figure 9.



(a) The forward speed at different times

(b) Recovery time under different types of disturbances

Fig. 9. Forward speed at different times and recovery time under various disturbance types

As shown in Figure 9(a), the forward speed of all three methods increased over time. When the time increased from 1.0s to 5.0s, the forward speed of the study method increased from 0.60 m/s to 1.20 m/s, an increase of 0.60 m/s. In the other two methods, when the time was 5.0s, the advancing speeds of MPC-WBC and Deep-RL were 0.85 m/s and 0.80 m/s respectively, which were significantly less than those of the study method. As shown in Figure 9(b), the recovery time of the study method was generally less than 2.0s in the face of different disturbance types, with a recovery time of 1.0s in the face of terrain vibration and 1.5s in the face of sudden load changes. The recovery times of the other two methods for each disturbance type were significantly longer than those of the study method. Overall, compared with the comparison methods, the study methods were better at coordinating limb movements, improving energy utilization efficiency, and had better perturbation suppression capabilities.

Table 4. Average forward speed and transportation cost under different manifold modulation gain parameters

Modulation gain parameter	Average forward speed (m/s)			Transportation cost		
	Research method	MPC-WBC	Deep-RL	Research method	MPC-WBC	Deep-RL
0	0.65	0.40	0.35	0.85	1.20	1.50
2	1.00	0.75	0.65	0.65	0.95	1.15
4	1.20	0.90	0.80	0.55	0.85	1.05
6	1.25	0.85	0.75	0.60	1.10	1.30
8	1.15	0.70	0.60	0.70	1.40	1.60
10	1.00	0.55	0.45	0.85	1.70	2.00

The average forward speed and transport cost of the three methods under different manifold modulation gain parameters were compared. Among them, transportation costs are defined as $\mathrm{CoT} = \frac{P_{\mathrm{avg}}}{mgv_{\mathrm{avg}}}$, where P_{avg} is average power, m is robot mass, g is gravitational acceleration, and v_{avg} is average forward speed. The average mechanical power is computed from Webots joint sensors as $P_{\mathrm{avg}} = \frac{1}{T}\int_0^T \sum_{j=1}^{n_j} \tau_j(t)\omega_j(t)dt$, where $\tau_j(t)$ is joint torque and $\omega_j(t)$ is joint angular

velocity. In Webots, joint torque and joint position are sampled at 1 kHz. The angular velocity is obtained by differentiating the joint position signal and filtering it with a second-order low-pass Butterworth filter at 50 Hz. The average forward speed is computed from base position displacement over the same time window. When electrical power is required, actuator electrical power is estimated as $P_{\text{elec}} = \frac{P_{\text{mech}}}{\eta_{\text{act}}} + P_{\text{idle}}$, where η_{act} is actuator efficiency from the motor datasheet and P_{idle} is idle electronic power. The reported CoT uses P_{avg} from mechanical power unless otherwise stated. The results are shown in Table 4.

As shown in Table 4, when the modulation gain parameter was within 10, the overall average forward speed of the study method at each parameter was greater than 0.65 m/s, and the overall transport cost was less than 0.85. When the modulation gain parameter was 6, the average forward speed reached a maximum of 1.25 m/s and the transport cost reached a minimum of 0.55. The average forward speed of the other two methods at each parameter was significantly lower than that of the study method, and the transport cost was significantly higher than that of the study method. Overall, the research method was more efficient in coordinating motion and energy distribution compared to the comparison method.

4.5 Sim-to-Real Transfer Risks and Hardware Validation Plan

The current experiments are conducted only in Webots. This simulation-only setting does not reproduce actuator torque saturation, gear backlash, communication latency, or friction uncertainty. These physical effects can alter phase tracking, contact force estimation, and the Hopf bifurcation threshold. The present results therefore provide simulation-level evidence rather than hardware-level validation.

Future work will use a physical quadruped platform. Actuator torque and joint velocity limits will be identified by bench tests. Gear backlash will be measured and included in the joint mapping. Communication delay will be modeled as a bounded input delay. Ground friction uncertainty will be represented by a friction cone with randomized contact parameters. Domain randomization will cover oscillator gains, contact stiffness, and terrain friction. Sim-to-real transfer will be evaluated by phase error, gait switching success rate, stability margin, and recovery time. Hardware-in-the-loop experiments will validate the proposed manifold modulation mechanism under unstructured terrain.

5. Conclusions

Aiming at the problems of abrupt multi-gait switching and the lack of a unified framework in the gait phase manifold modulation of existing quadruped robots, this study innovatively proposed a gait phase manifold modulation mechanism for quadruped robots based on nonlinear differential geometry and Hopf bifurcation analysis. The study constructed a CPG-Hopf oscillator network and introducing contact force feedback, defined limiting circulation shapes and geodesic distances, and used bifurcations to drive manifold topological transitions. Phase resilience analysis of the manifold modulation strategy under terrain changes showed median phase error vector amplitudes of the study method on flat land, gravel, slopes, and steps were 2.5%, 3.3%, 4.0%, and 2.9%, respectively. Analysis of gait switching and control accuracy in unstructured terrain showed that the success rate of gait switching of the study method was 99.9%, 98.7%, 97.5%, and 96.0% respectively when the terrain was flat, gravel, slope, and steps. The stability margin was 11.0 cm at 25 percent gait cycle and 7.9 cm at 90 percent gait cycle. The overall roll angle error at each time was less than 1.5°, and the overall pitch angle error was less than 1.8°. The overall performance analysis of the modulation mechanism showed that when the time increased from 1.0 s to 5.0 s, the forward speed of the study method increased from 0.60 m/s to 1.20 m/s. Its overall recovery time in the face of different perturbation types was less than 2.0 s. When the modulation gain parameter was within 10, the overall average forward speed at each parameter was greater than 0.65 m/s, and the overall transport cost was less than 0.85. The results showed that the proposed method in the study could not only effectively deal with terrain change scenarios, but also maintain high control accuracy during gait switching, and had good feasibility and superiority. However, the current study did not explore the gait control performance of the robot in a dynamic environment.

Future work will extend the experimental range, combine online learning algorithms for gait parameter optimization, and conduct physical hardware experiments to address actuator limits, gear backlash, communication latency, and friction uncertainty.

Acknowledgments

The research is supported by the Fourth Phase of the Ministry of Education's Supply-Demand Matching Employment and Education Integration Project: Application-Oriented and Project-Based Teaching of University Mathematics and Interdisciplinary Talent Cultivation (Project No.: 2024102110581).

References

[1] Azeez SA, Mandava RK, Naik NS. A Novel Review on Quadruped Robots Design Variants, Gait Modulation, and Motion Planning Schemes. Journal of Field Robotics. 2025;42(7):3615-3693. https://doi.org/10.1002/rob.22575

[2] Calzolari D, Della Santina C, Albu-Schaffer A. Exciting families of passive gaits in an elastic quadruped via natural motion manifold control. The International Journal of Robotics Research. 2026;45(2):233-258. https://doi.org/10.1177/02783649251347305

[3] Li Q, Qian L, Wang S, Sun P, Luo X. Towards generation and transition of diverse gaits for quadrupedal robots based on trajectory optimization and whole-body impedance control. IEEE Robotics and Automation Letters. 2023;8(4):2389-2396. https://doi.org/10.1109/LRA.2023.3251184

[4] Song Y, Peng Y, Zhang T. Double Hopf bifurcation analysis in the memory-based diffusion system. Journal of Dynamics and Differential Equations. 2024;36(2):1635-1676. https://doi.org/10.1007/s10884-022-10180-z

[5] Guo J, Shi H, Zeng J, Li T. Double-parameter Hopf bifurcation analysis of a high-speed rail vehicle with an alternative wheel/rail contact Approximation. Vehicle System Dynamics. 2023;61(2):530-549. https://doi.org/10.1080/00423114.2022.2050770

[6] Prasad HKH, Hatton RL, Jayaram K. Geometrically modulable gait design for quadrupeds. IEEE Robotics and Automation Letters. 2024;9(8):7142-7149. https://doi.org/10.1109/LRA.2024.3418311

[7] Song Z, Zhu J, Xu J. Gaits generation of quadruped locomotion for the CPG controller by the delay-coupled VDP oscillators. Nonlinear Dynamics. 2023;111(19):18461-18479. https://doi.org/10.1007/s11071-023-08783-2

[8] Liu X, Wu J, Xue Y, Qi C, Xin G, Gao F. Skill latent space based multigait learning for a legged robot. IEEE Transactions on Industrial Electronics. 2024;72(2):1743-1752. https://doi.org/10.1109/TIE.2024.3429576

[9] Chen C, Xiang P, Zhang J, Xiong R, Wang Y, Lu H. Deep reinforcement learning based co-optimization of morphology and gait for small-scale legged robot. IEEE/ASME Transactions on Mechatronics. 2023;29(4):2697-2708. https://doi.org/10.1109/TMECH.2023.3330427

[10] Huang Y, Li Y, Liu G, Li D, Rob L, Zhu L, Wu EQ. Terrain Perception and Stiffness Adaptation-Based Attitude Control for Quadruped Robots. IEEE/ASME Transactions on Mechatronics. 2025;30(6):6821-6833. https://doi.org/10.1109/TMECH.2025.3528031

[11] Khazoom C, Hong S, Chignoli M, Stanger-Jones E, Kim S. Tailoring solution accuracy for fast whole-body model predictive control of legged robots. IEEE Robotics and Automation Letters. 2024;9(12):11074-11081. https://doi.org/10.1109/LRA.2024.3455907

[12] Xu W, Sen W, Xing L, Da Z, Jin H, Xin X, Bin D, Qiguang M. Deep Reinforcement Learning: A Survey. IEEE Transactions on Neural Networks and Learning Systems. 2024;35(4):5064-5078. https://doi.org/10.1109/TNNLS.2022.3207346

[13] Eclerova V, Pribylova L, Botha AE. Embedding nonlinear systems with two or more harmonic phase terms near the Hopf–Hopf bifurcation. Nonlinear Dynamics. 2023;111(2):1537-1551. https://doi.org/10.1007/s11071-022-07906-5

[14] Liu D, Jiang W. Steady-state bifurcation and Hopf bifurcation in a reaction–diffusion–advection system with delay effect. Journal of Dynamics and Differential Equations. 2024;36(2):1777-1817. https://doi.org/10.1007/s10884-022-10231-5

[15] Mustafa SA, Hussen NH. Hopf and Zero-Hopf Bifurcation of the Four-Dimensional Lotka-Volterra Systems. Baghdad Science Journal. 2025;22(2):605-622. https://doi.org/10.21123/bsj.2024.9456

[16] Shaik J, Uchida TK, Vyasarayani CP. Nonlinear dynamics near a double Hopf bifurcation for a ship model with time-delay control. Nonlinear Dynamics. 2023;111(23):21441-21460. https://doi.org/10.1007/s11071-023-08965-y

[17] Achouri H, Aouiti C. Explicit formulas for calculating the normal form of zero-Hopf bifurcation in a class of neutral differential equations. Journal of Mathematical Sciences. 2025;289(5):725-748. https://doi.org/10.1007/s10958-024-07400-w

[18] Yu X, Song Z, Sun X, Xu J. A Theoretical Approach for Gait Generation of the CPG Controller by Using the Time-Delay Coupled Oscillators. SIAM Journal on Applied Dynamical Systems. 2026;25(1):518-553. https://doi.org/10.1137/25M1739820
[19] Kalmar-Nagy T, Horvath DA. Numerical Hopf normal form for delay-differential equations. Nonlinear Dynamics. 2025;113(13):16383-16399. https://doi.org/10.1007/s11071-025-10958-y
[20] Hahm C, Jay R. Testing the Effects of Evolved Central Pattern Generators in an Articulated Robot Animat Ecosystem. Journal of Climbing and Walking Robots. 2026. https://doi.org/10.47852/bonviewJCWR62027653
[21] Hassan M, Fayomi O, Faust J, Mahajan A. A Bio-inspired Climbing Robot with Directional Dry Adhesion for Reduced-Gravity Mobility. Journal of Climbing and Walking Robots. 2025. https://doi.org/10.47852/bonviewJCWR52026892
[22] Alidousti J, Salehi K, Eskandari Z. Bifurcation analysis of Duffing oscillator with a fifth-order nonlinear factor. International Journal of Modelling and Simulation. 2025;45(4):1286-1298. https://doi.org/10.1080/02286203.2023.2273620